



# Meteorological Data from KLAWS-2G for an Astronomical Site Survey of Dome A, Antarctica

Yi Hu<sup>1</sup>, Keliang Hu<sup>1</sup>, Zhaohui Shang<sup>2,1</sup>, Michael C. B. Ashley<sup>3</sup>, Bin Ma<sup>1</sup>, Fujia Du<sup>4</sup>, Zhengyang Li<sup>4</sup>, Qiang Liu<sup>1</sup>, Wei Wang<sup>1</sup>, Shihai Yang<sup>4</sup>, Ce Yu<sup>5</sup>, and Zhen Zeng<sup>1</sup>

<sup>1</sup>National Astronomical Observatories, Chinese Academy of Sciences, Beijing, 100101, People's Republic of China

<sup>2</sup>Tianjin Normal University, Tianjin, 300387, People's Republic of China; [zshang@gmail.com](mailto:zshang@gmail.com)

<sup>3</sup>School of Physics, University of New South Wales, NSW 2052, Australia

<sup>4</sup>National Astronomical Observatories, Nanjing Institute of Astronomical Optics & Technology, Chinese Academy of Sciences, Nanjing, 210042, People's Republic of China

<sup>5</sup>College of Intelligence and Computing, Tianjin University, Tianjin, 300072, People's Republic of China

Received 2018 September 7; accepted 2018 October 12; published 2018 November 27

## Abstract

We present an analysis of meteorological data from the second generation of the Kunlun Automated Weather Station (KLAWS-2G) at Dome A, Antarctica during 2015 and 2016. We find that a strong temperature inversion exists for all the elevations up to 14 m that KLAWS-2G can reach, and lasts for more than 10 hours for 50% or more of the time when temperature inversion occurs. The average wind speeds at 4 m elevation are  $4.2 \text{ m s}^{-1}$  and  $3.8 \text{ m s}^{-1}$  during 2015 and 2016, respectively. The strong temperature inversion and moderate wind speed lead to a shallow turbulent boundary layer height at Dome A. By analyzing the temperature and wind shear profiles, we note telescopes should be elevated by at least 8 m above the ice. We also find that the duration of temperature inversions and the wind speed vary considerably from year to year. Therefore, long-term and continuous data are still needed for the site survey at Dome A.

*Key words:* site testing – atmospheric effects – methods: data analysis

*Online material:* color figures

## 1. Introduction

The Antarctic plateau has long been thought to contain the best sites on earth for many astronomical observations. The most promising and well studied candidates include Dome A, Dome C, Dome Fuji, and Ridge A. By reviewing the available data for these sites from ground-based instruments, satellites, and numerical simulations, Saunders et al. (2009) and Burton (2010) summarized their weather conditions, boundary layer heights, atmospheric seeing, clouds, aurorae, etc. These studies showed excellent astronomical observing conditions at all four Antarctic sites, superior in many cases to the best lower-latitude sites, such as Mauna Kea.

Long-term and in situ measurement data are essential to draw robust conclusions on the astronomical sites. For Dome C, Lawrence et al. (2004) reported a median free-atmospheric seeing of  $0.23''$  above a boundary layer just less than 30 m high, based on data from a multi-aperture scintillation sensor (MASS) and a sonic radar (SODAR). Aristidi et al. (2005) analyzed two decades of temperature and wind speed data from an automated weather station and four summers of measurements with balloon-borne sondes, and found that Dome C had an extremely stable upper atmosphere and a very low inversion layer. Travouillon et al. (2008) used balloon-borne measurements to find that the median

value of the boundary layer height at Dome C is 33 m. Aristidi et al. (2009) obtained a median seeing of  $1.67''$  at 3 m, dropping to  $0.84''$  at 20 m based on 3.5 years of differential image motion monitor (DIMM) data.

Up until now, only Dome C among the sites mentioned above has had a regular manned operation over winter. Because of logistical difficulties, the other potential sites lack long-term and continuous data.

For Dome A, Bonner et al. (2010) reported a median boundary layer height of 13.9 m using seven months of data obtained in 2009 from the Snodar instrument, a sonic radar giving 1 m resolution up to 200 m above the ice. By analyzing eight months of data from the first Kunlun automated weather station (KLAWS), Hu et al. (2014, hereafter HU14) found a strong and long-lasting temperature inversion existing just above the snow surface, and an anti-correlation between the temperature inversion strength and the boundary layer height.

For Dome Fuji, Okita et al. (2013) reported a  $0.53''$  seeing at 11 m, and a  $0.2''$  seeing when the boundary layer height was lower than 11 m. However, the time span of their data was only 18 days during 2013 January.

Mast-based automated weather stations (AWS), such as KLAWS, with multiple sensors at different elevations are important for site evaluation. Not only can a mast AWS give

direct information on the atmospheric turbulence and wind speed below the boundary layer (HU14), it can also provide crucial data for site simulations (Falvey & Rojo 2016). Moreover, it has helped us to operate unattended telescopes (Shang et al. 2012; Liu et al. 2018) at Dome A, and the data are also useful for designing and building large diameter telescopes with adaptive optics systems (Aristidi et al. 2005) in the future.

In this paper, we present the results from analyzing continuous data spanning one year and eight months from KLAWS-2G. Instrumentation and sensor calibration are described in Section 2. A statistical analysis of temperature, wind speed, and relative humidity data and a comparison with data from the first generation AWS are presented in Sections 3 and 4. Finally, a discussion and summary is presented in Section 5.

## 2. Instrument and Calibration

### 2.1. Instrumentation

Our second-generation weather station KLAWS-2G (see Figure 1) was installed at Dome A in 2015 January by the 31st Chinese National Antarctica Research Expedition (CHINARE) team. KLAWS-2G has a 15 m high mast, the same height as that of the first generation KLAWS (HU14). The mast supports 10 temperature sensors, at heights of  $-1$  m (i.e., below the ice level), 0, 1, 2, 4, 6, 8, 10, 12, and 14 m, seven wind speed and direction sensors (at 2, 4, 6, 8, 10, 12, and 14 m), one air pressure sensor (at 2 m), and one relative humidity sensor (at 2 m). Temperatures are measured with 4-wire resistance temperature detectors (RTD) (Young Model 41342). Wind speeds and directions are measured with propeller anemometers (Young Wind Monitor-AQ model 05305V). Air pressure is measured with a barometric pressure sensor (Young Model 61302V). Relative humidity is measured with a relative humidity/temperature probe (Young Model 41382 VC). A custom data acquisition electronic box sits at the foot of the mast. The electronic box is connected to the controlling and operating system of the Antarctic Survey Telescope (AST3) via an RS232 cable (Shang et al. 2012). The main computer of AST3 acquired the data from all the sensors every 10 seconds and transferred them to the data server at our institute every 15 minutes via Iridium satellite. The temperatures are read directly from the sensors, and other measurements are read as voltage values and then transformed to their actual values using the formulae given by the manufacturer. Power and Internet connectivity for KLAWS-2G, and a warm operating environment for the computers, was provided by Plateau Observatory A (PLATO-A), an automated observatory (Lawrence et al. 2008) installed in 2012.

KLAWS-2G operated continuously from January 2015 to August 2016. During that time, all of the sensors worked well, apart for the barometer which suffered from ice accumulation. Some other problems developed over time. The radiation shield



**Figure 1.** KLAWS-2G installed at Dome A in 2015 January. The temperature sensors (in the radiation shields) and anemometers are clearly visible. The electronic box sits at the foot of the mast. The photo was taken in 2016. (A color version of this figure is available in the online journal.)

of the temperature sensor at 10 m was broken since 2015 October 3, for there was an abrupt change in the behavior of the sensor. Later at the end of 2016 August, we found that the temperature inversion disappeared above 6 m, and our webcam of KLAWS-2G saw the mast was bent at about 5 m, indicating damage to the mast and some sensors. KLAWS-2G stopped working completely on 2016 September 9, caused by the failure of the serial port server device. In 2017 January, KLAWS-2G was maintained by the 33rd CHINARE team, the serial port server device was replaced by a new one and all the sensors at 4 m and below were resumed. The team also installed a new identical electronic box of KLAWS-2G to replace the old one. At this time, we placed a new barometer (Vaisala PTB2010 B2B4A) inside the electronics box rather than directly exposing it outside. From 2017 January until

PLATO-A’s kerosene supply ran out in 2018 May, all of the sensors up to 4 m, including the new barometer, worked very well.

## 2.2. Calibration

Platinum RTDs are widely used in weather stations, due to their stability and accuracy. Converting from resistance to temperature for a “standard” RTD is usually done using the Callendar-Van Dusen equation, or, for the highest accuracy, using the international standard ITS-90 (Preston-Thomas 1990). The measurement range defined in the standard reaches from  $-259\text{ }^{\circ}\text{C}$  to  $+961\text{ }^{\circ}\text{C}$ . Our Young 41342 temperature sensor slightly differs from the standard RTD, and the manufacturer specifies a measurement range from  $-50\text{ }^{\circ}\text{C}$  to  $+50\text{ }^{\circ}\text{C}$ . As the actual temperature at Dome A was usually considerably below  $-50\text{ }^{\circ}\text{C}$ , especially in wintertime (see HU14), we sent three Young 41342 sensors to National Institute of Metrology, China (NIM) for calibrating in 2016. One of the three temperature sensors was purchased in 2014 and was from the same batch of sensors used for KLAWS-2G. The other two were purchased in 2015 from another production run. These calibrations allowed us to investigate both the zero shift and consistency of Young 40342 Model temperature sensors when used outside their nominal working temperature range.

The results from NIM include the requested calibrating temperatures, the actual calibrating temperatures and the measured resistances of our sensors, which can be converted to the temperatures our sensors would read. The calibration results are tabulated in Table 1. The actual calibration temperature (column 3) in each experiment was not strictly equal to that we requested (column 2). NIM used a standard high precision RTD to measure the actual temperature. All the expanded uncertainties of standard temperature are  $0.02\text{ }^{\circ}\text{C}$ , where the coverage factor  $k = 2$ , which are also provided by NIM. Expanded uncertainty and coverage factor are explained in detail by Mohr et al. (2016). The temperatures measured by our temperature sensors can be calculated using the formula in Table 1. Figure 2 shows the temperature differences between those from the standard RTD and those measured by these three sensors. The maximum difference is  $+0.18\text{ }^{\circ}\text{C}$  under the  $-70\text{ }^{\circ}\text{C}$  experiment, which is from the sensor we purchased in 2014. Compared with the calibration results of the two sensors we purchased in 2015, the maximum difference is only  $0.05\text{ }^{\circ}\text{C}$ , while the maximum difference between the two batches is  $0.15\text{ }^{\circ}\text{C}$ . We note that the temperatures measured by the sensor purchased in 2014 are systematically larger than those measured by the sensors purchased in 2015, which might be caused by a zero shift. In conclusion, the consistency among the same batch of Young 41342 is better than  $0.05\text{ }^{\circ}\text{C}$  and the zero shift of this type of RTD between different batch should be less than  $0.15\text{ }^{\circ}\text{C}$ . The resistance to temperature formula can be safely expanded to  $-80\text{ }^{\circ}\text{C}$  with a less than  $0.1\text{ }^{\circ}\text{C}$  accuracy.

**Table 1**  
Young Model 41342 Temperature Sensor Calibration Results

Serial No.	Set ( $^{\circ}\text{C}$ )	Actual ( $^{\circ}\text{C}$ )	Resistance ( $\Omega$ )	Read ( $^{\circ}\text{C}$ )
(1)	(2)	(3)	(4)	(5)
024705 (2014)	$-40.0$	$-40.016$	846.921	$-39.91$
	$-50.0$	$-50.008$	808.526	$-49.83$
	$-60.0$	$-59.997$	769.761	$-59.82$
	$-70.0$	$-70.008$	730.777	$-69.83$
026881 (2015)	$-40.0$	$-40.014$	846.654	$-39.98$
	$-50.0$	$-50.006$	808.276	$-49.90$
	$-60.0$	$-59.997$	769.358	$-59.93$
	$-70.0$	$-70.007$	730.365	$-69.94$
026883 (2015)	$-40.0$	$-40.019$	846.422	$-40.04$
	$-50.0$	$-50.010$	808.212	$-49.92$
	$-60.0$	$-59.995$	769.217	$-59.96$
	$-70.0$	$-70.012$	730.185	$-69.98$

**Note.** Column 1 is the sensor serial number and date of manufacture. Column 2 is the temperature that we requested for each experiment. Column 3 is the actual temperature of the experiment as measured by NIM’s standard RTD. Column 4 is the resistance measured by NIM. Column 5 is the temperature converted from column 4 using the transfer function provided by the manufacturer:  $T(^{\circ}\text{C}) = A \cdot R^2(\Omega) + B \cdot R(\Omega) + C$ ,  $A = 1.1279 \times 10^{-5}$ ,  $B = 2.3985 \times 10^{-1}$ ,  $C = -251.1326$ , where T is the temperature in Celsius, and R is the resistance in ohms.

Therefore, we conclude that the Young Model 41342 is safe for using at Dome A.

We also sent three anemometers to NIM for calibration. Since the size of the wind tunnel available at NIM was comparable to the anemometer size, we did not obtain absolute calibration results. However, we were still able to confirm the linearity of the transfer function of the Young 05305V anemometers. The calibration results are tabulated and showed in Table 2 and in Figure 3. As shown in Figure 3, except for the lowest two wind speeds, the voltages measured under the same experiments are all roughly two-thirds of the expected values calculated using the conversion formula given by the manufacturer. This is caused by the effect of the air stream in the wind tube being partially blocked by the body of the anemometer. Throughout this text, we will use the transfer function provided by the manufacturer to obtain the actual wind speed.

## 2.3. Data Caveats

We note a few problems in the data that readers should be aware of in understanding the data and results below.

The radiation shield of the temperature sensor at 10 m dropped off on 2015 October 3. After this time, the temperature measured by the sensor at 10 m is higher than the true value, as we will show in Section 3.1. We use a corrected temperature at

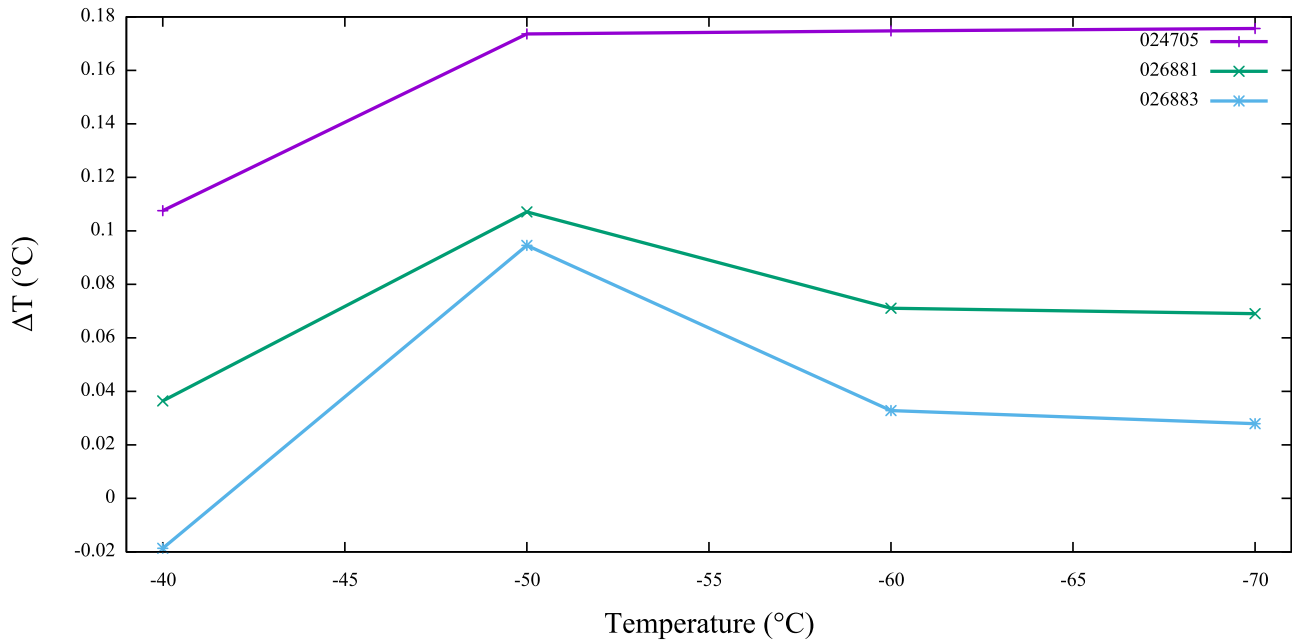


**Figure 2.** Temperature differences between the actual temperature (column 3 in Table 1) and the read temperature (column 5 Table 1). (A color version of this figure is available in the online journal.)

**Table 2**  
Young Model 41342 Wind Speed Sensor Calibration Results

Serial No.	Wind speed [m s <sup>-1</sup> ]	Measured [mV]	Expected [mV]
(1)	(2)	(3)	(4)
132885 (2014)	1.00	29	50
	2.00	68	100
	5.00	165	250
	10.00	348	500
	15.00	514	750
	20.00	689	1000
	25.00	852	1250
143509 (2015)	1.00	47	50
	2.00	85	100
	5.00	183	250
	10.00	373	500
	15.00	545	750
	20.00	707	1000
	25.00	866	1250
148412 (2015)	1.00	47	50
	2.00	87	100
	5.00	188	250
	10.00	396	500
	15.00	535	750
	20.00	703	1000
	25.00	868	1250

**Note.** Column 4 is the expected voltage converted from column 2 using the transfer function provided by the manufacturer:  $V = kU$ ,  $k = 0.02$ , where  $V$  is the wind speed in m s<sup>-1</sup>, and  $U$  is the voltage in mV.

10 m after 2015 October 1 for calculating temperature gradient at heights of 10 m and 12 m (see Section 3.1).

According to the anemometer's user manual, there is a narrow blind spot in wind direction to the north. Also, because of blocking by the mast body, the measured wind speed, when the wind direction is near due east or west, is smaller than the true speed, as we will show in Section 3.2. This is also why there is a gap in the wind rose plots.

The relative humidity sensor's working temperature is only specified to work from  $-50$  °C to  $+50$  °C. Therefore, the relative humidity could be underestimated from its true value when the ambient temperature is lower than  $-50$  °C. There are more details on this issue in Section 3.3.

The barometer only worked correctly for one month during 2016, as the result of problems mentioned in Section 2.1. In this paper, we do not present air pressure data.

### 3. Data Statistics and Results

#### 3.1. Temperature and Temperature Inversion

To show the long-term trend within an entire year, we plot the daily median temperatures in 2015 and 2016 in Figure 4. Taking 2 m as an example, the daily median temperature at 2 m in 2015 was approximately  $-35$  °C from January to February, then dramatically went down to roughly  $-60$  °C in April, and could frequently reach below  $-70$  °C in the dark winter. It rose again after October when the polar night was over. The daily median temperature above the surface could vary more than

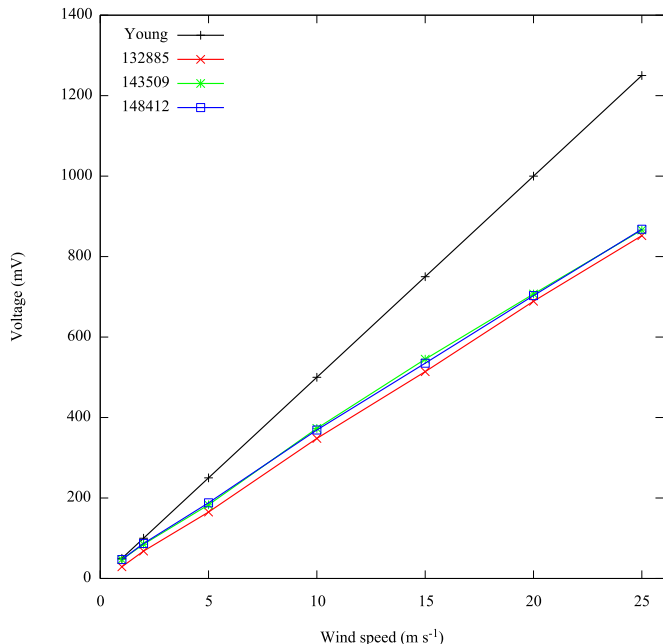


**Figure 3.** Calibration results of the anemometers. The black line labeled as “Young” is the transfer function in Table 2. The data also come from Table 2. (A color version of this figure is available in the online journal.)

10 °C in two days, but the daily median temperature at  $-1$  m (1 m below the surface) varied smoothly because thick loose snow covers the ground surface at Dome A and isolates heat transmission. Because of the good thermal insulation of the loose snow, the temperature at  $-1$  m is lower than the surface temperature in summer and higher in the winter (Figure 4). The same trend can also be seen in the 2011 data (see Figure 7 in HU14).

We show the detailed temperature distributions of  $-1$  m and surface (0 m) in Figure 5. The temperature at  $-1$  m in both years has a much smaller range (from  $-70$  °C to  $-40$  °C) than the air temperature (from  $-80$  °C to  $-25$  °C), as we had seen in 2011 (HU14). We note that the surface air temperature could reach below  $-80$  °C in 2015 and 2016.

The temperature distributions of the other elevations are shown in Figures 6 and 7. We can see there are shallow valleys between  $-50$  °C and  $-40$  °C in these temperature distribution figures. It divides the data into three components: the long cold winter, the warm summer, and the valley where the temperatures changed relatively rapidly during spring and autumn as we have seen in Figure 4. The valleys are more obvious in 2016 than those in 2015, because the data after 2016 September were absent, while the rapid changing of temperature in spring and autumn is not symmetric.

To investigate annual variation, we list the 25%, 50% and 75% monthly percentiles at 4 m during 2015 and 2016 in Table 3 and plot them in Figure 8. The monthly percentiles in

2016 are lower than those in 2015, except in May and August. This suggests that the temperature in 2016 was lower than that in 2015, but the month-to-month median temperature can vary as much as 5 °C.

The temperature inversion (i.e., temperature decreasing with increasing elevation), can be clearly seen in Figure 4, as we also saw in 2011 (HU14). The temperature gradients are calculated and shown in Figures 9 and 10. Note that we calculate the temperature gradient at a given height from the temperature difference between that height and the adjacent lower height, divided by the height difference. For example, the gradient at 8 m is  $(T(8\text{ m}) - T(6\text{ m}))/2$ . A positive gradient indicates a temperature inversion.

As we have seen in Figure 4, the temperature at 10 m became the highest from 2015 November until 2016 March, when the Sun started to set below the horizon. We noticed this in early 2015 October, and inferred that this is not real and it could be that the radiation shield of the temperature sensor at 10 m was broken or dropped off. This was confirmed by the 32nd CHINARE team in early 2016, but it could not be fixed on site. For this reason, hereafter we calculated the temperature gradient at 10 m assuming that the variation was linear from 8 to 12 m. The plots all show a very strong temperature inversion that the gradient distributions increase rapidly from negative values to a narrow positive peak and go down with a relatively long tail.

When the temperature inversion happens, it can last a long time. To quantify how long the temperature inversion can last, we first define a real temperature inversion by adopting the criteria of temperature difference larger than 0.14 °C as we did in HU14. This is because that the temperature sensors are from the same batch of production, according to the calibration results presented in Section 2.2, it is reasonable to regard that a temperature difference larger than 0.14 °C is a real measurement, rather than random measurement error or systematic zero shift between two temperature sensors. Then the inversion lasting time is defined as a time period in which all the temperature differences are equal or larger than 0.14 °C. The cumulative distribution of temperature inversion lasting time are listed in Table 4 and shown in Figure 11. For all the heights, more than 50% of the time, the temperature inversion could last more than 10 hours. The longest temperature inversion was 6 days at 4 m elevation in 2015.

### 3.2. Wind Speed and Wind Direction

The daily median wind speeds in 2015 and 2016 are shown in Figure 12. Unlike for the temperature, there were no obvious seasonal trends of wind speed. However, the wind speed in the winter season (from April to September) is larger than that in the summer season (from October to March). For example, the average wind speed at 4 m in the summer of 2015 was  $4.0\text{ m s}^{-1}$ , while it was  $4.5\text{ m s}^{-1}$  in the winter. The average wind speeds at 4 m during 2015 and 2016 were  $4.2\text{ m s}^{-1}$  and

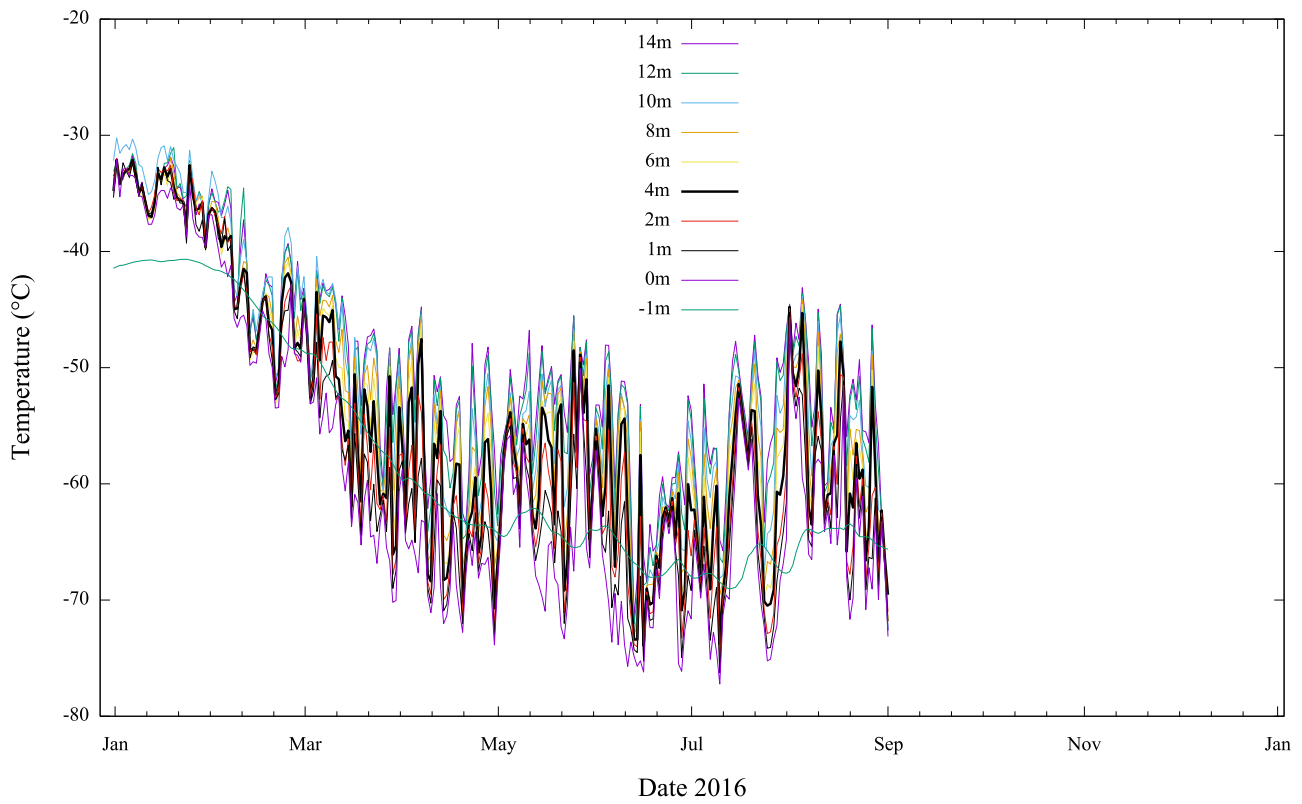
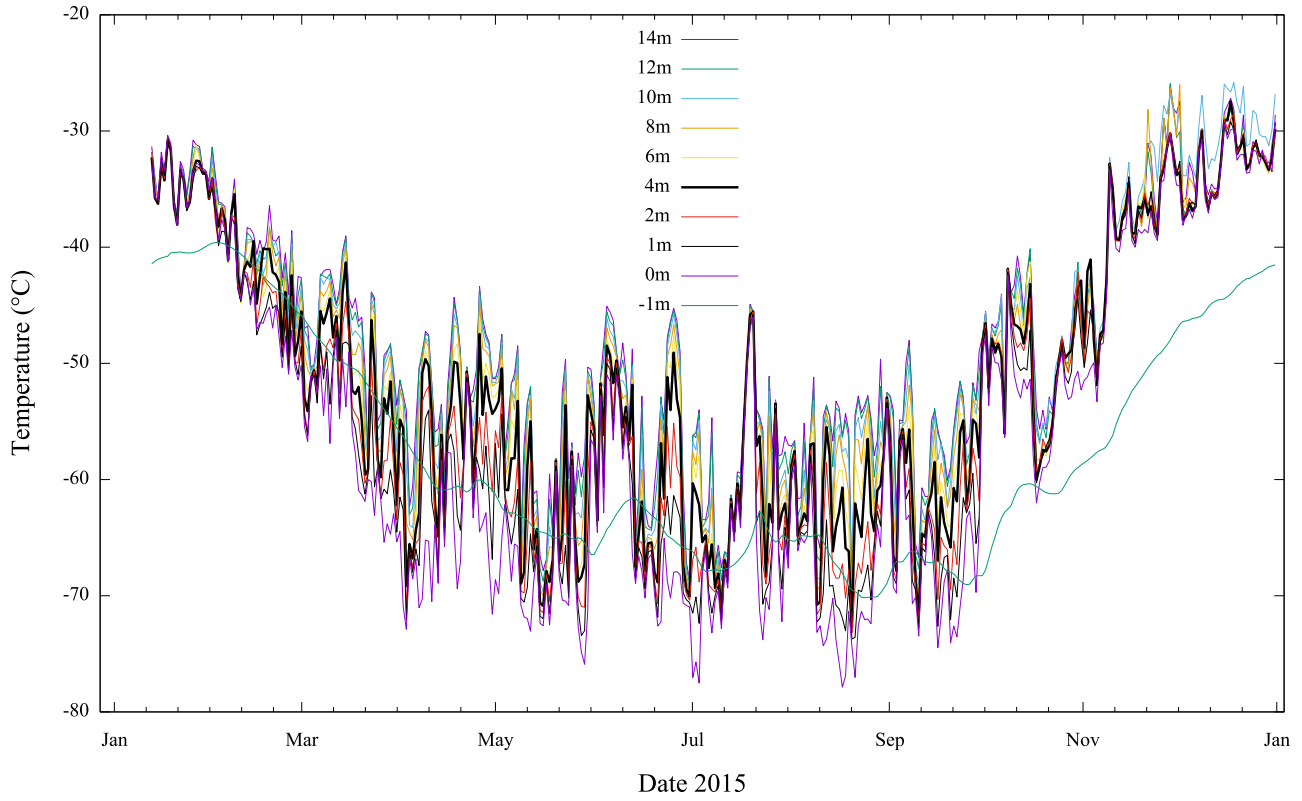


**Figure 4.** Daily temperature median during 2015 and 2016.  
(A color version of this figure is available in the online journal.)

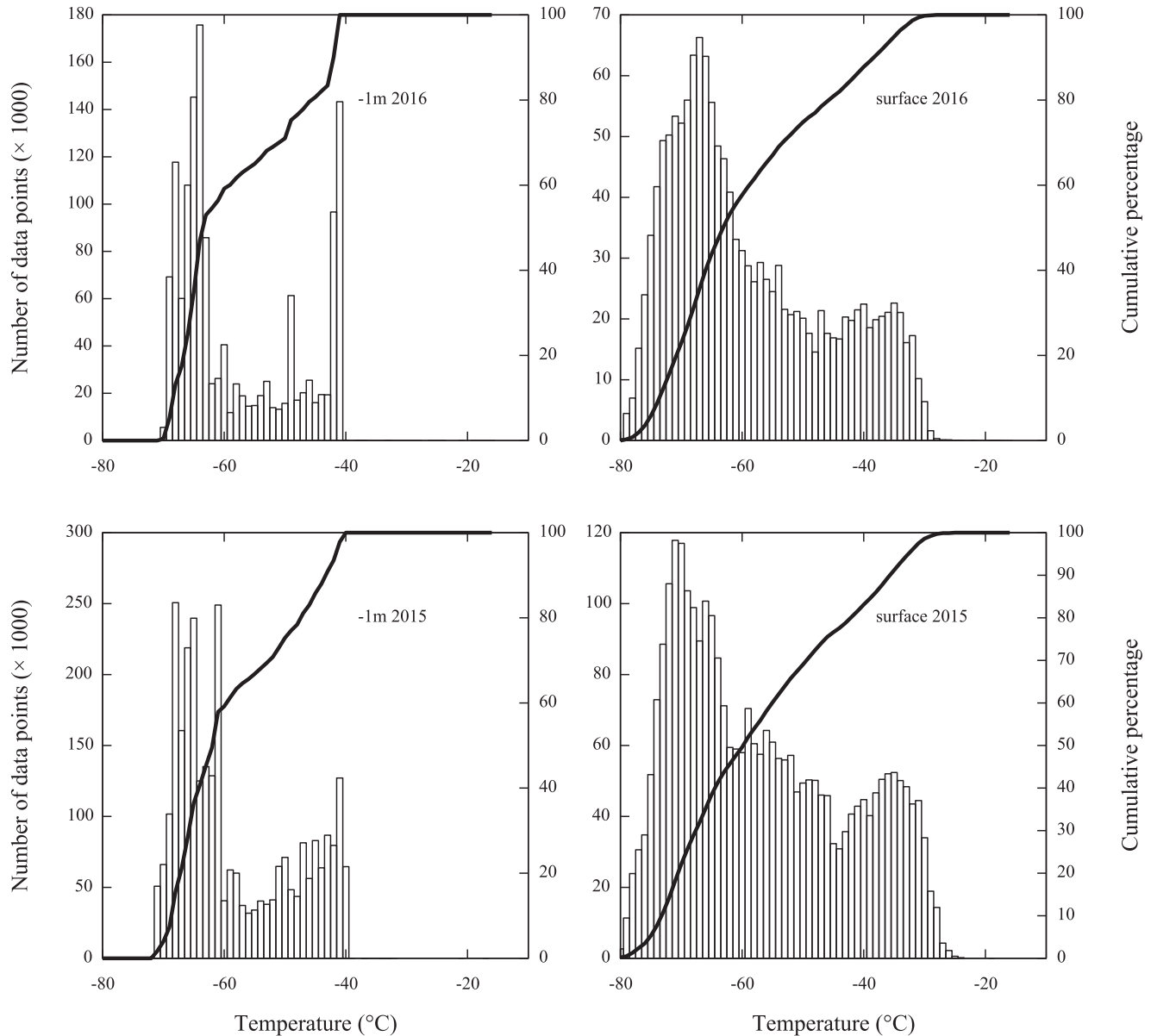


**Figure 5.** Histograms and cumulative distributions (solid line) of the temperatures of surface and 1 m under the surface during 2015 and 2016.

$3.8 \text{ m s}^{-1}$ , respectively. In general, higher elevations have higher wind speeds. Sometimes the daily wind speed was recorded as zero (see Figure 12). This occurred, for example, during a few days in 2015 July for the sensor at 12 m. We infer that such extended periods of zero readings are usually not real, but probably caused by the anemometer being frozen after a period of very low wind speed. As seen in Figure 12, when the wind speed at a certain elevation is almost zero and those at other elevations were not zero at the same time, we always found that after a strong wind, the anemometer with problem

could recover, indicating that it got stuck (possibly frozen) during a low wind speed period.

The wind speed distribution during 2015 and 2016 are shown in Figures 13 and 14. The distributions of wind speed at all the elevations show an asymmetric peak, whose position depends on its corresponding height.

We note that there could be more low wind speed points, especially the zero wind speed points, than there should be, because the anemometer might be partially frozen when the wind speed is low, but we cannot quantify this effect.

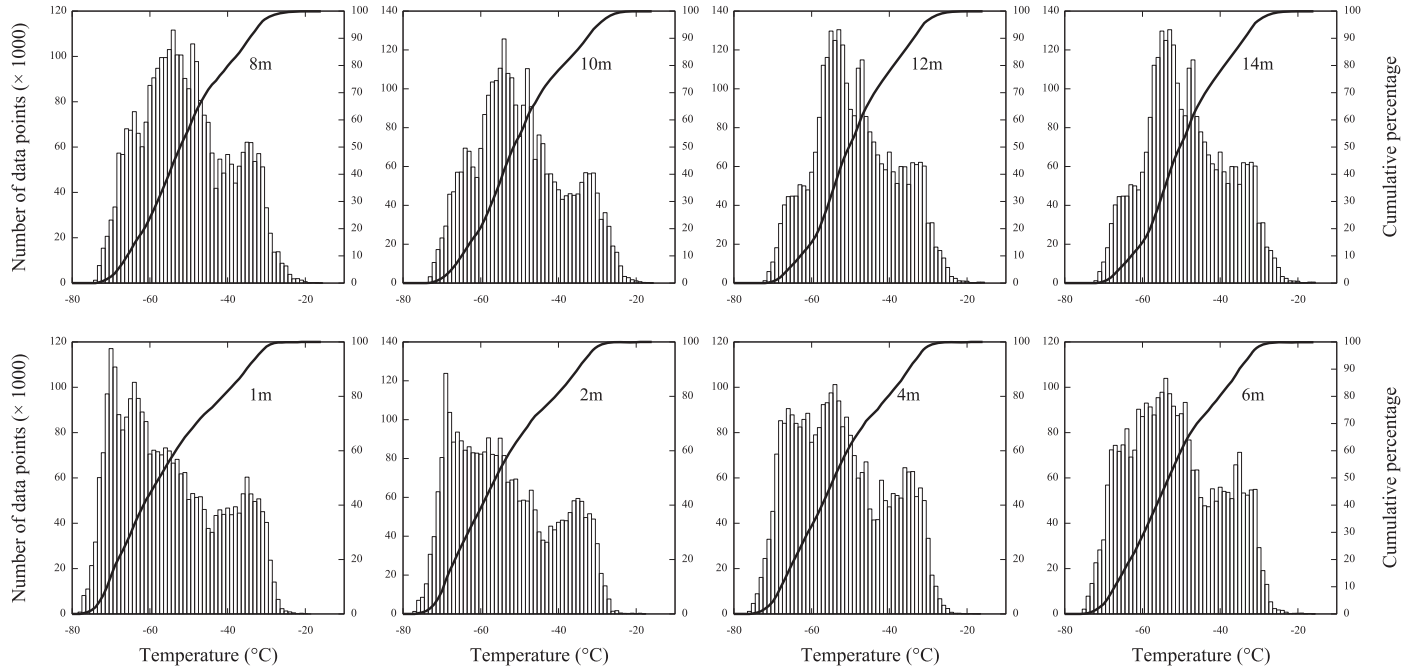


Figure 6. Histograms and cumulative distributions (solid line) of the temperatures from 1 m to 14 m during 2015.

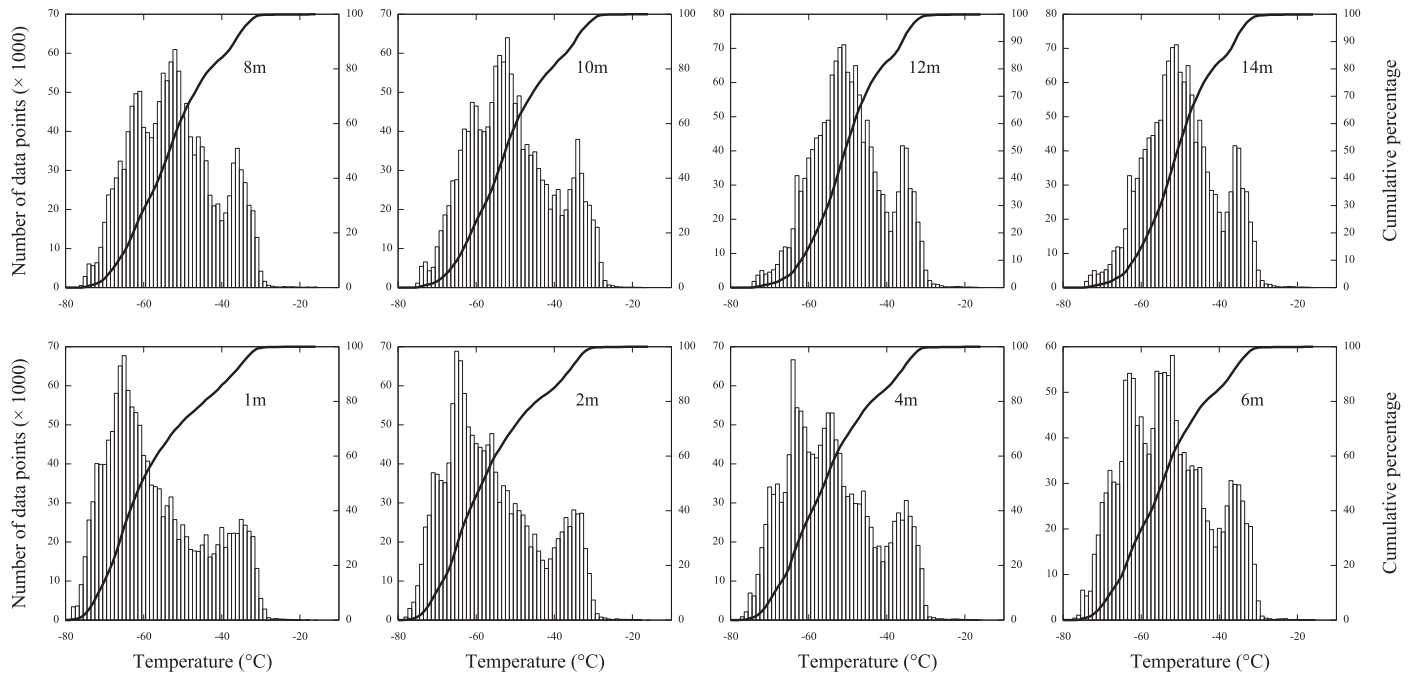


Figure 7. Histograms and cumulative distributions (solid line) of the temperatures from 1 m to 14 m during 2016.

Although a higher elevation has a higher wind speed, the wind speeds for all the elevations seldom exceeded  $10 \text{ m s}^{-1}$ , which is a great advantage for astronomical observatories.

The wind rose plots in 2015 and 2016 are shown in Figures 15 and 16. There is a very narrow “blind” spot to the north in wind

direction as we mentioned in Section 2.3. There are also gaps to the east or west directions which are caused by mast blocking. The direction of the gap is depended on position of the corresponding anemometer. The wind rose density plots show there is a slightly preferred southeast wind direction, at about  $150^\circ$ .



**Table 3**  
Monthly Percentile Temperature at 4 m During 2015 and 2016

Month	25%		50%		75%	
	(2015)	(2016)	(2015)	(2016)	(2015)	(2016)
Jan	-37.38	-37.03	-34.34	-34.62	-31.80	-32.53
Feb	-46.80	-48.42	-43.23	-44.71	-39.26	-41.20
Mar	-58.17	-60.02	-53.64	-54.99	-48.76	-49.55
Apr	-64.38	-67.86	-57.98	-63.98	-54.35	-60.29
May	-69.12	-63.52	-65.03	-59.06	-59.11	-56.04
Jun	-66.50	-70.38	-60.64	-65.88	-54.83	-62.49
Jul	-68.44	-69.83	-65.69	-64.94	-60.77	-61.11
Aug	-68.42	-64.48	-64.98	-59.44	-61.14	-52.84
Sep	-67.60	...	-63.14	...	-58.58	...
Oct	-54.01	...	-50.00	...	-45.62	...
Nov	-42.75	...	-38.22	...	-33.77	...
Dec	-35.59	...	-33.08	...	-30.37	...

### 3.3. Relative Humidity

According to the World Meteorological Organization, relative humidity is defined as the ratio of water vapor pressure and saturated water vapor pressure over water under that temperature, regardless of whether the temperature is larger than the freezing point of water (Hardy 1998a). Our relative humidity sensor gives measurements conforming to WMO’s definition, according to its manual. However, we did not calibrate our humidity sensor due to the lack of a suitable experimental chamber that can provide a very dry, low air pressure and low-temperature environment.

Figure 17 shows the daily median relative humidity during 2015 and 2016. It is clear that the relative humidity has the same trend as the temperature (see Figure 4). In the summer the relative humidity could be as high as 65%, while in the winter it could drop to 35%. The air near the ground on the Antarctic plateau is usually super-saturated, i.e., the “standard” relative humidity is larger than 100% (Hardy 1998a). On 2015 February 3, the daily median temperature was  $-38.90^{\circ}\text{C}$  and the daily median relative humidity was 60.1%. This corresponds to “standard” relative humidity of nearly 100%, because using Table 2 in Hardy (1998a), when the “standard” relative humidity is 100%, the relative humidity defined by WMO at  $-38.90^{\circ}\text{C}$  is 68%.

Figure 18 shows a strong correlation between the relative humidity and the temperature at 2 m. It is obvious that there is a turnover near  $-50^{\circ}\text{C}$  in Figure 18. Based on its working principle, the humidity sensor measures the absolute water content in the air, and then translates the measurement to relative humidity by calculating the saturated water vapor pressure under the ambient temperature (Hardy 1998b). Our relative humidity sensor has its own temperature sensor; however, its measurement range is fixed from  $-50^{\circ}\text{C}$  to  $+50^{\circ}\text{C}$ . When the ambient temperature is lower than  $-50^{\circ}\text{C}$ ,

the temperature that it reads is still  $-50^{\circ}\text{C}$ . This will overestimate the saturated water vapor pressure and thus result in an underestimated relative humidity. However, despite the turnover, the strong correlation shown in Figure 18 still indicates a nearly 100% “standard” relative humidity all the time at least for ambient temperature higher than  $-40^{\circ}\text{C}$ , and this is probably also true for lower temperature.

## 4. Comparison between 2011 (KLAWS) and 2015–2016 (KLAWS-2G) Data

We have collected and analyzed meteorological data from ground to 14 m high at Dome A for about three years, in 2011 with KLAWS and 2015–2016 with KLAWS-2G. We compare the results to have a better understanding of the site as a potential astronomical observatory.

The daily median temperatures for all the elevation above 0 m at Dome A decrease rapidly from January to April as the Sun sets lower and lower, become quasi-constant during polar nights from May to September (although the day to day median temperature variation could be as large as more than  $10^{\circ}\text{C}$ ), and finally rapidly go up from October to December. This trend is stable at Dome A and can be clearly seen in Figure 4 during 2015 and 2016 and Figure 2 in HU14 during 2011. The same trend had been found at South Pole (Hudson & Brandt 2005) and Dome C (Aristidi et al. 2005). The average temperatures of the first seven months at 2 m and 14 m are  $-54^{\circ}\text{C}$  and  $-46^{\circ}\text{C}$ ;  $-54^{\circ}\text{C}$  and  $-48^{\circ}\text{C}$ ; and  $-55^{\circ}\text{C}$  and  $-49^{\circ}\text{C}$  during 2011, 2015, and 2016, respectively. This seems very consistent year to year. However, the surface temperature at 0 m during 2015 and 2016 could reach below  $-80^{\circ}\text{C}$  rarely for less than 0.1% of the time, but this had never been seen in 2011 (HU14).

The annual average wind speed at 4 m in 2015 and 2016 are  $4.2\text{ m s}^{-1}$  and  $3.8\text{ m s}^{-1}$ , respectively, much higher than that at the same elevation in 2011, which is only  $1.5\text{ m s}^{-1}$ . Although the anemometer occasionally got stuck in 2011, resulting in a smaller average wind speed, this problem could not change the average wind speed by a factor of three. Therefore, we believe that this difference reflects the annual climatological change. Another difference is that the wind direction exhibits a slightly preferred wind direction of  $150^{\circ}$  during 2015 and 2016, while there was no preferred wind direction during 2011.

Comparing with the results we obtained in 2011 (HU14), the total fractions of time when temperature inversion existed above 4 m in 2015–2016 is 10% to 40% smaller than those in 2011 (see Tables 4 and 1 in HU14). The percentages of time when temperature inversion duration time exceeded 25 hr in 2015 are about 20% smaller than those in 2011. On the ice cap of Antarctic continent, the temperature inversion is driven by the difference in emissivity between the snow surface and air. It can be destroyed by the strong force of wind shear or net downward shortwave radiation flux (Vignon et al. 2017). Therefore, one possible reason that the temperature inversion

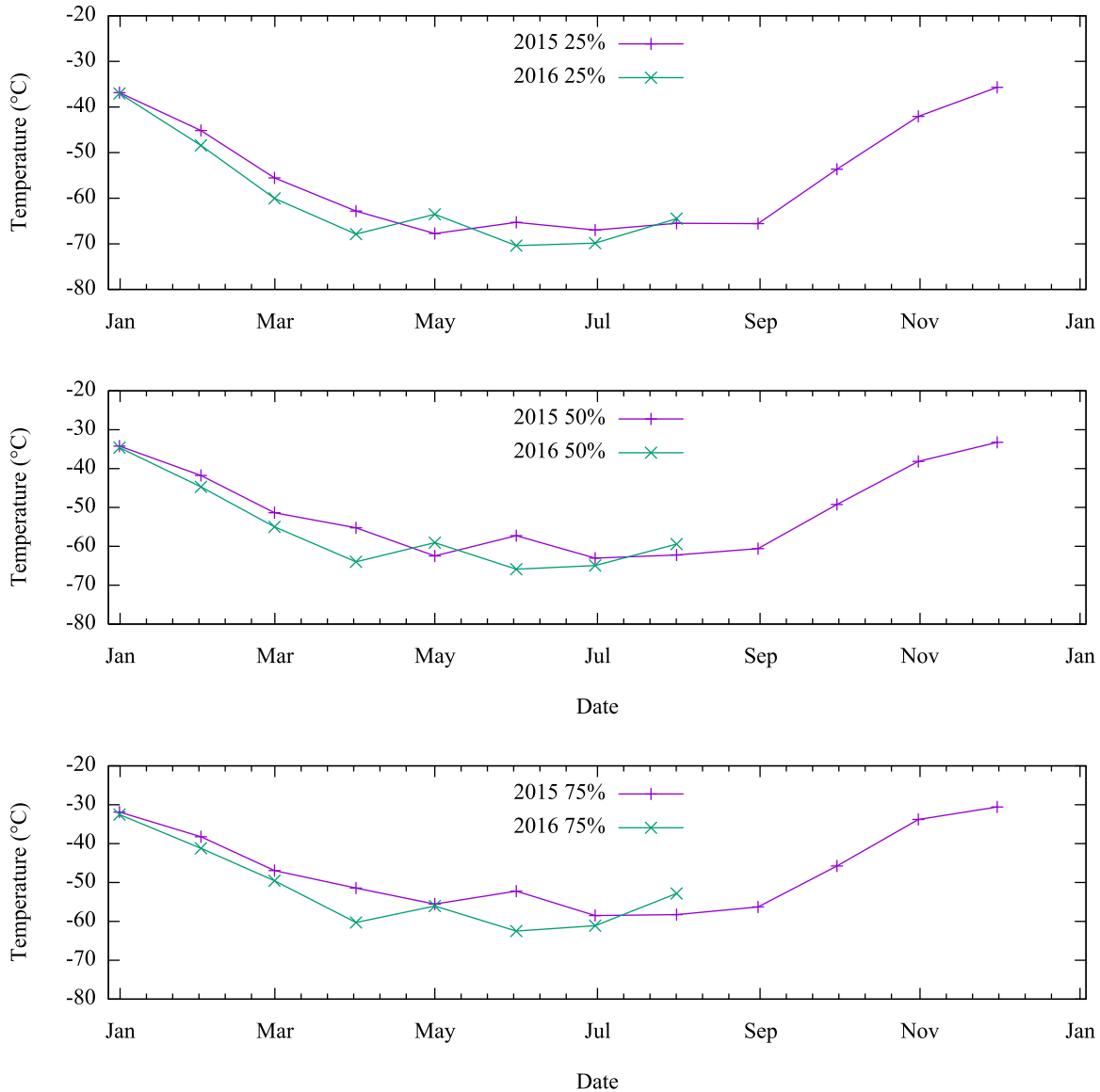


**Figure 8.** Monthly 25%, 50%, and 75% percentile temperature of 4 m in 2015 and 2016. (A color version of this figure is available in the online journal.)

durations in 2015–2016 are shorter is the higher wind speeds in 2015–2016 than in 2011. However, we cannot rule out that the cloudy skies were more frequent during 2015–2016, which also generate net downward radiation flux, and thus destroy the temperature inversion. The large difference in temperature inversion statistics between 2015–2016 and 2011 shows that the meteorological parameters are quite variable from year to year. Such annual variations in temperature inversions were also observed by Zhou et al. (2009).

To show the annual variation in temperature inversion, we plot the monthly median temperature difference at 4 m (e.g.,  $T(4\text{ m}) - T(2\text{ m})$ ) during 2015, 2016 and 2011 in Figure 19.

The monthly temperature difference at 4 m during these three years could vary within a wide range up to 2 °C, especially in the winter season.

Similar to HU14, we show the monthly median temperature difference at 4 m in 2015 and boundary layer heights in 2009 (Bonner et al. 2010) in Figure 20. The anti-correlation is not as obvious as we had found in 2011 (Figure 22 in HU14). This could attribute to the yearly variation (see Figure 19).

Finally, we plot median temperature gradient profile and median wind speed gradient profile in Figure 21. We note that the temperature gradients at 10 m and 12 m was obtained using corrected 10 m temperature (see Section 3.1). Temperature

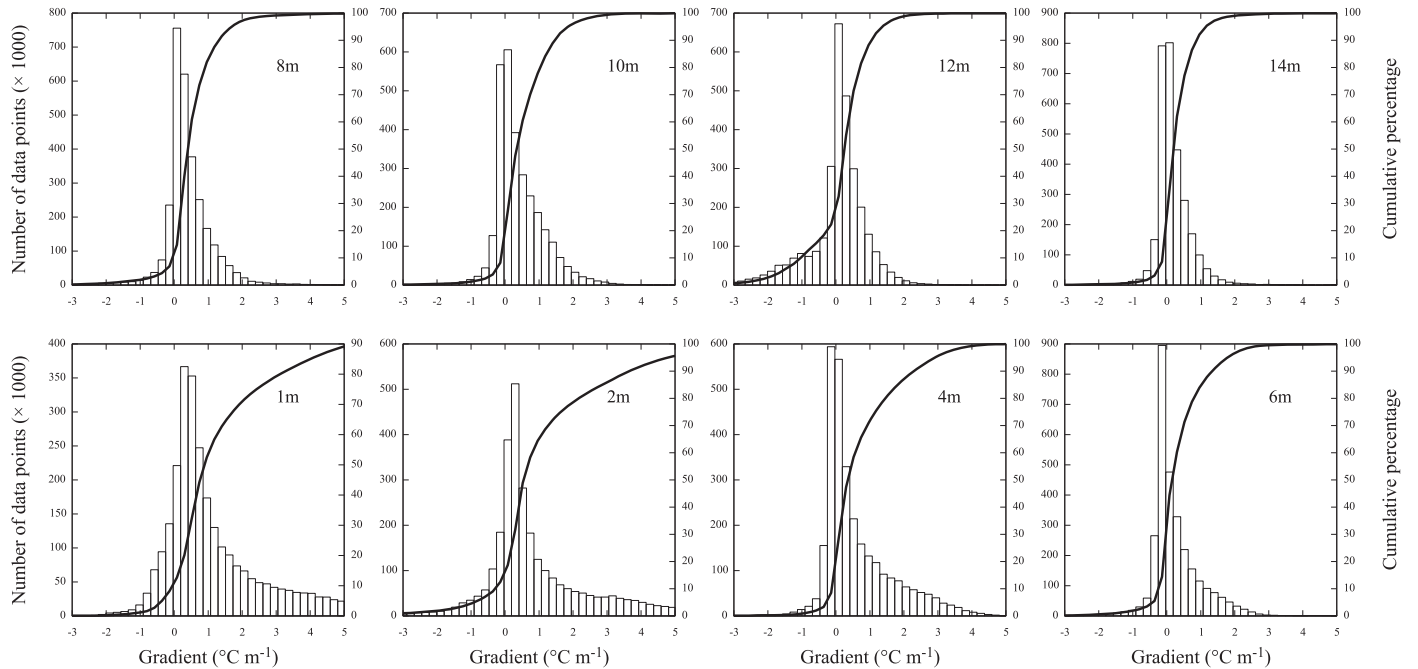


**Figure 9.** Histograms and cumulative distributions (solid line) of the temperature gradients from 1 m to 14 m during 2015. The temperature gradients are calculated by corrected temperature at 10 m after 2015 October 1 (see Section 3.1).

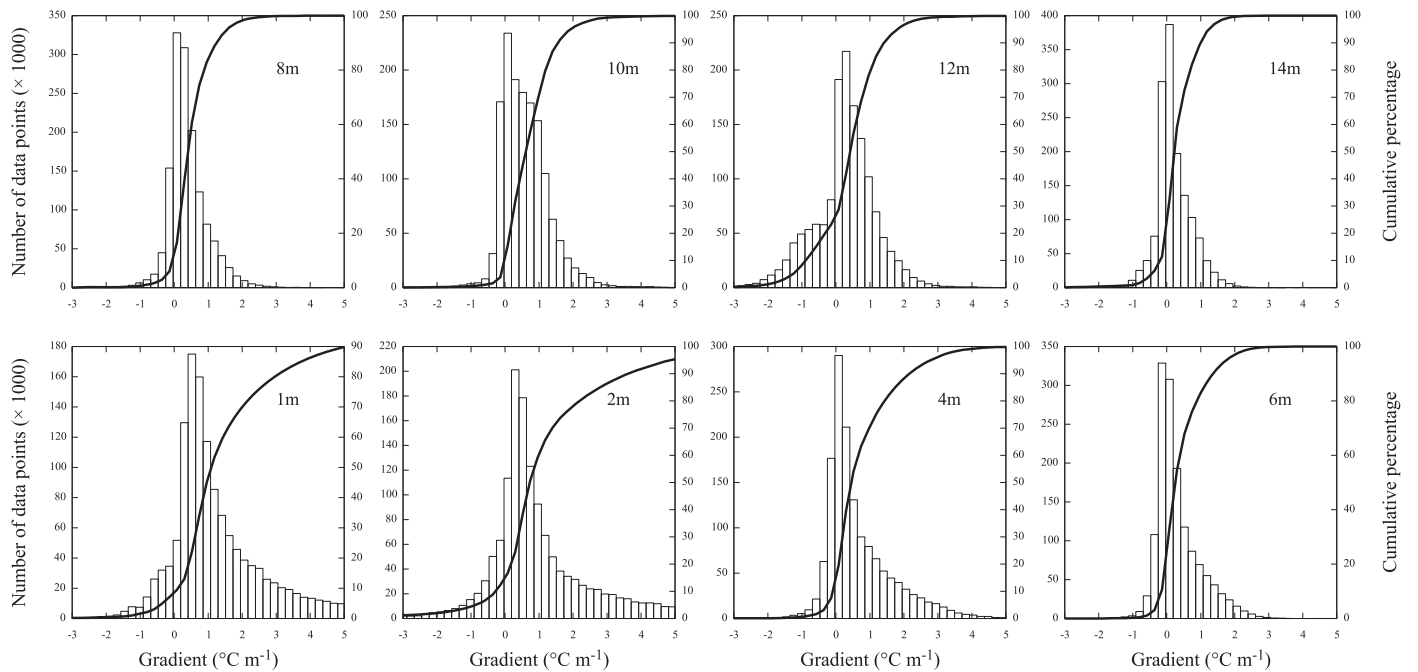


**Figure 10.** Histograms and cumulative distributions (solid line) of the temperature gradients from 1 m to 14 m during 2016. The temperature gradients are calculated by corrected temperature at 10 m. The temperature gradients are calculated by corrected temperature at 10 m (see Section 3.1).

gradient profiles in 2015 and 2016 exhibit similar behavior at the lower elevations, while the profile in 2011 is completely different. The temperature gradients decrease dramatically from 1 m to 6 m in 2015 and 2016, and then increase moderately at 8 m. The wind

speed gradient profiles also have such turnover at 6 m (see right panel in Figure 21). However, both temperature gradient and wind speed gradient above 8 m asymptotically approach positive constant values, at least in 2011 and 2015.

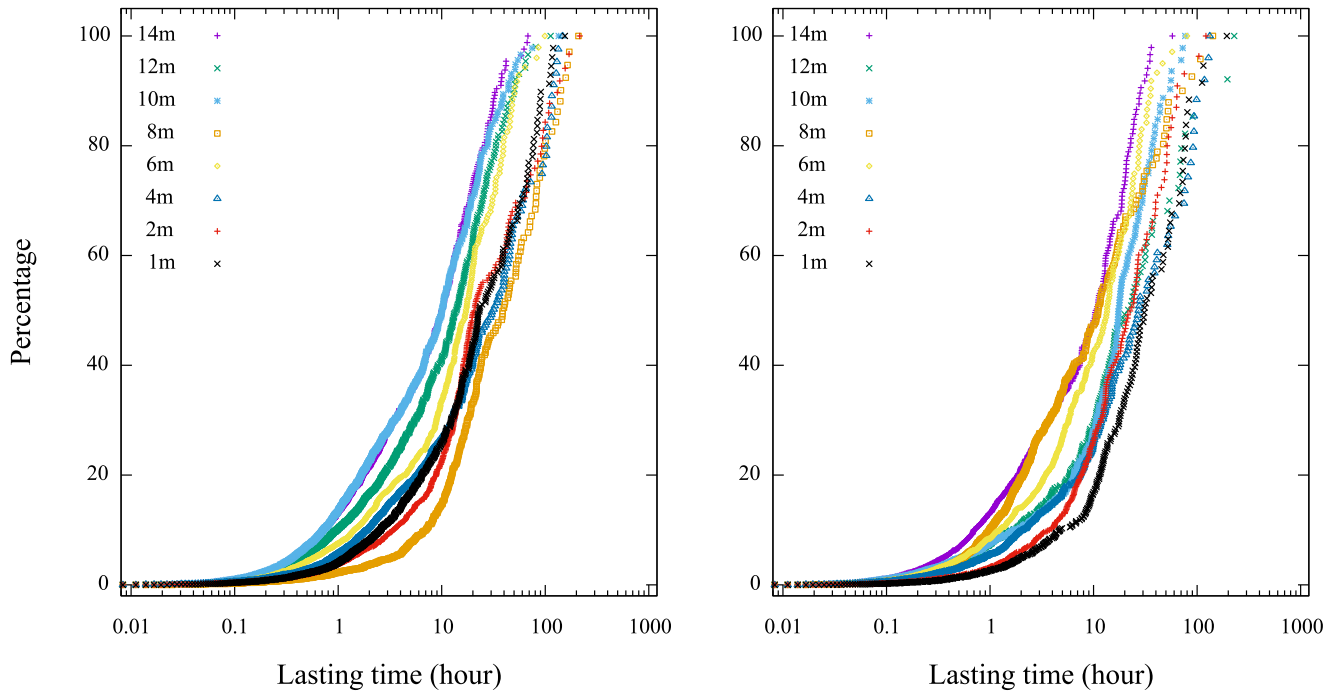


**Figure 11.** Temperature inversion duration time during 2015 (left panel) and 2016 (right panel). The temperature gradients are calculated by corrected temperature at 10 m after 2015 October 1.

(A color version of this figure is available in the online journal.)

**Table 4**  
Cumulative Percentages of the Durations of Temperature Inversion

Height (m)	>10 hr		>25 hr		Total	
	%(2015)	%(2016)	%(2015)	%(2016)	%(2015)	%(2016)
1	74.1	83.4	48.9	60.3	85.7	89.8
2	77.5	73.7	45.3	47.1	79.2	81.8
4	73.0	73.9	53.6	53.2	72.7	81.4
6	66.4	57.8	34.9	25.1	56.6	66.8
8	85.5	52.7	58.5	31.5	85.9	84.1
10	45.0	79.8	18.0	58.8	63.1	88.0
12	62.7	79.8	30.1	58.7	73.9	88.0
14	50.0	51.9	20.1	15.2	66.5	69.3

## 5. Summary and Discussion

By analyzing data collected from KLAWS-2G at Dome A during 2015 and 2016, we find that the temperature seems to have a similar seasonal trend from year to year, which is reasonable. The average wind speed at 4 m in 2015–2016 was around  $4 \text{ m s}^{-1}$ , much higher than that ( $1.5 \text{ m s}^{-1}$ ) in 2011. Nevertheless, these are still very low wind speeds compared with that at temperate astronomical observatories. Unlike in 2011, there was a slightly preferable wind direction of  $150^\circ$  in 2015–2016. All the differences indicate the existence of annual variations in the meteorological parameters at Dome A.

Most importantly, we have still found there is a very strong temperature inversion (temperature gradient reaching up to  $7 \text{ }^\circ\text{C m}^{-1}$  at 4 m) at all the heights above the snow surface, confirming our results in 2011 (HU14). Our calibration results of the temperature sensors in Section 2.2 have proved that such a temperature inversion, as we defined as positive temperature difference larger than  $0.14 \text{ }^\circ\text{C}$ , is a real phenomenon rather than inconsistency between temperature sensors. Whenever a temperature inversion exists, competition between shear and buoyancy will weaken turbulence and result in a shallower boundary layer. Thus, the atmospheric seeing will probably

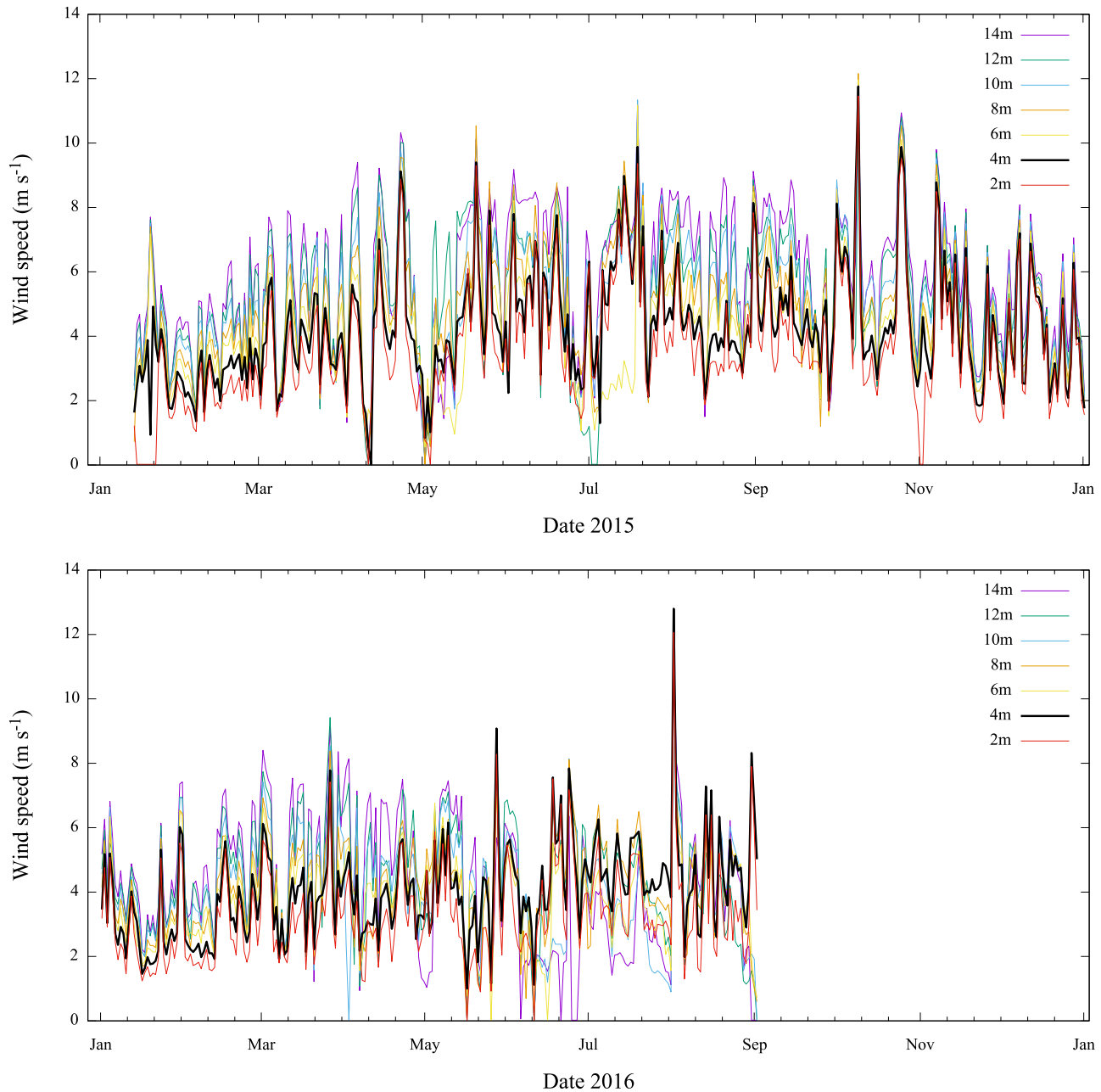


**Figure 12.** Daily median wind speed during 2015 and 2016.  
(A color version of this figure is available in the online journal.)

become better when temperature inversion occurs. We have also built a similar AWS and installed it at Muztagata site in Pamirs Plateau in April 2017. DIMMs have been installed at that site for directly measuring atmospheric seeing. Although temperature inversion is not as frequent or strong as that at Dome A, when it exists, the seeing is usually better (private communication).

By studying meteorological data at Dome C, Vignon et al. (2017) claimed that the stable boundary layer (SBL) could be

divided into two regimes with respect to the wind speed at 10 m. In the first regime, the wind speed is strong, associated with continuous turbulence. In the second regime, the wind speed is weak, the temperature inversion is strong, thus the turbulent activity is weak. Figure 22 shows the relation between wind speed and temperature gradient at 4 m in 2015. It is clear that there is a wind speed threshold roughly around  $6.0 \text{ m s}^{-1}$ . Below the threshold, the temperature gradients are scattered over a very wide range and could reach as large as

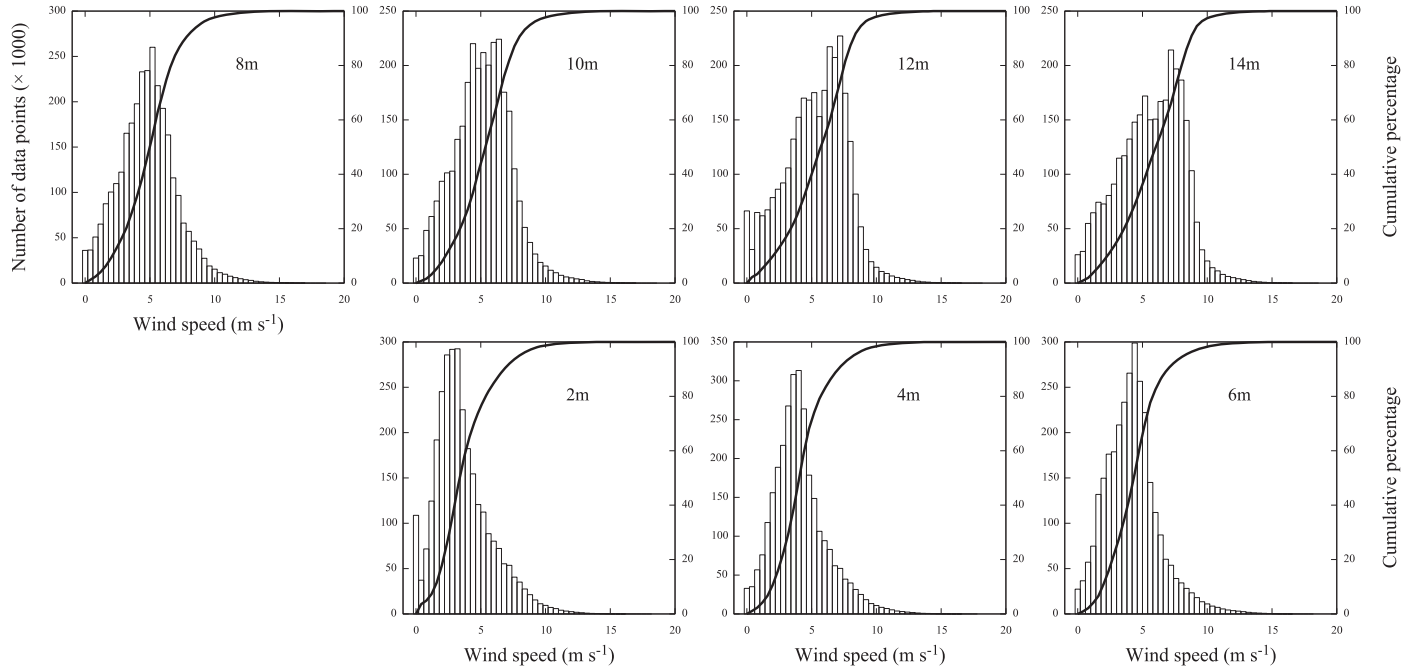


**Figure 13.** Histograms and cumulative distributions (solid line) of wind speeds from 2 m to 14 m during 2015.

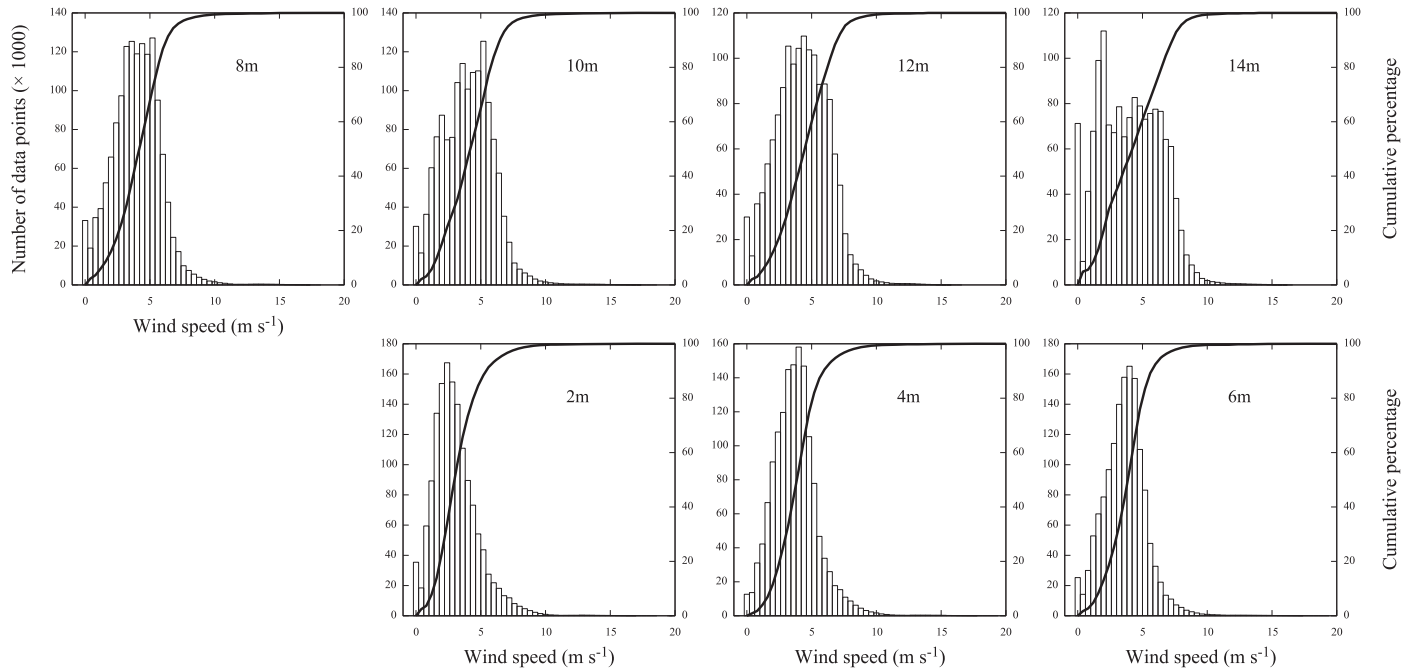


**Figure 14.** Histograms and cumulative distributions (solid line) of wind speeds from 2 m to 14 m during 2016.

$7\text{ }^{\circ}\text{C m}^{-1}$ . When the wind speeds are stronger than  $6.0\text{ m s}^{-1}$ , the temperature gradients are moderate and their absolute values slightly decrease with the wind speed. The relation between wind speed and temperature gradient in Figure 22

implies that there are also two distinct SBL regimes at Dome A which could be characterized by the local wind speed.

Large atmospheric seeing within a narrow turbulent boundary layer is ubiquitous on Antarctica continent, as

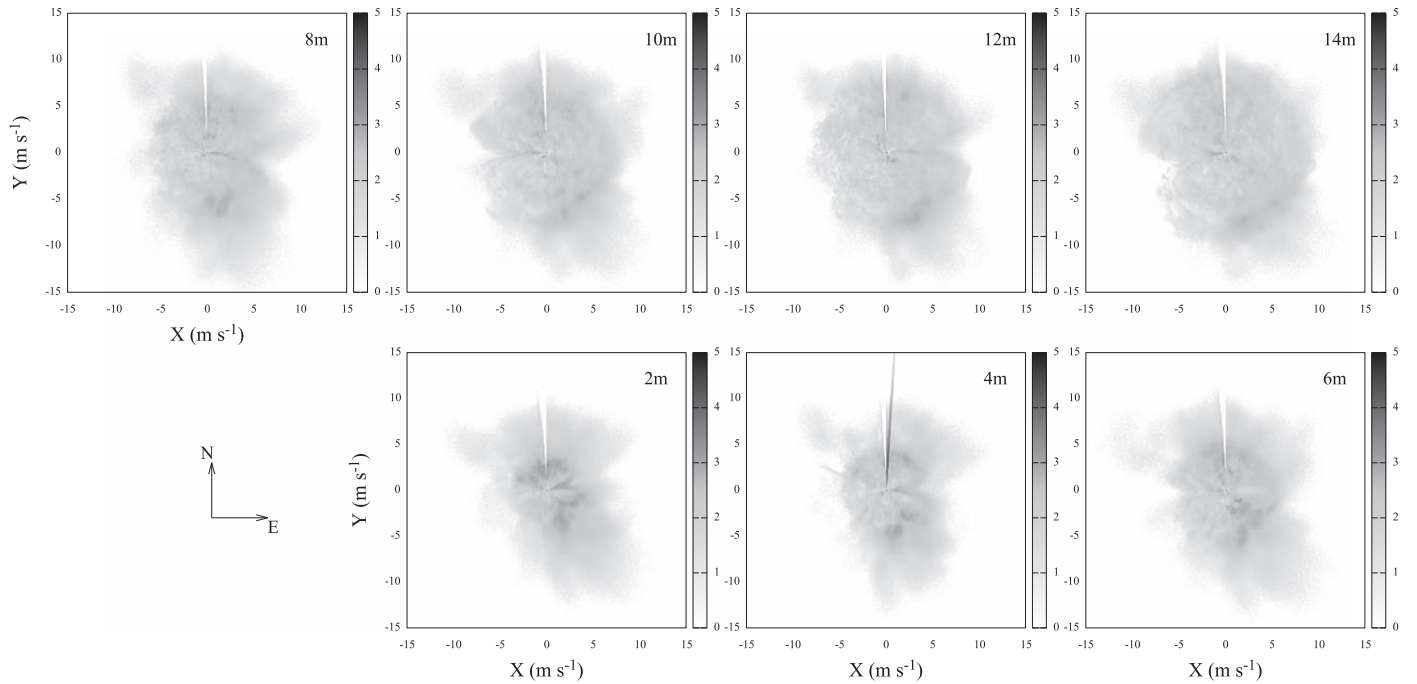


**Figure 15.** Wind rose density at seven heights during 2015. The gray scale is the logarithm of the number of data points in each pixel. The blind strips to the north are caused by an imperfection in the acquisition module (see Section 3.2 for details). The gaps to the east or west are caused by mast blocking.

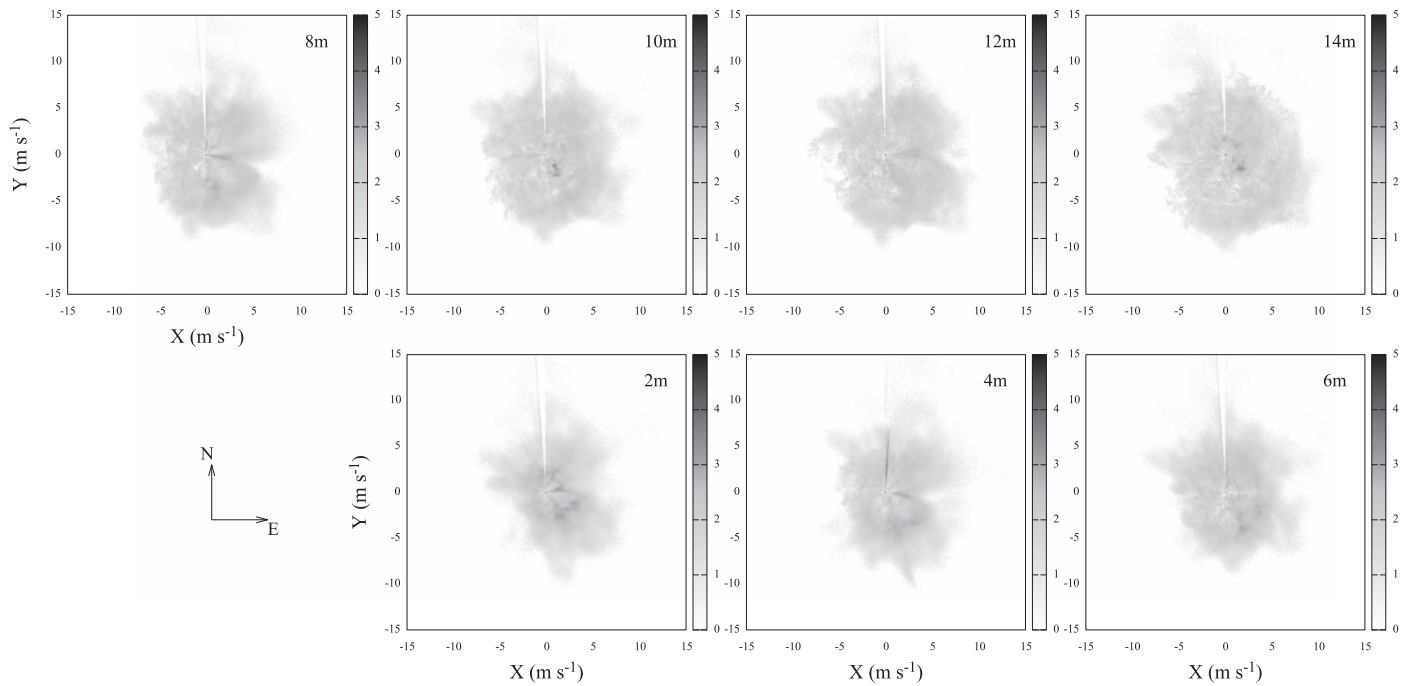


**Figure 16.** Same figure as Figure 15, but during 2016.

observed, e.g., by Marks et al. (1996) and Aristidi et al. (2009), and theoretically studied by Swain & Gallée (2006). Therefore, a telescope should be sited above the boundary layer to avoid the strong turbulence in the ground layer. Vignon et al. (2017)

found the temperature profile near the ground was a convex-concave-convex shape in the first SBL regime at Dome C and an exponential shape in the second SBL regime. However, the median temperature gradient profile at Dome A (left panel in

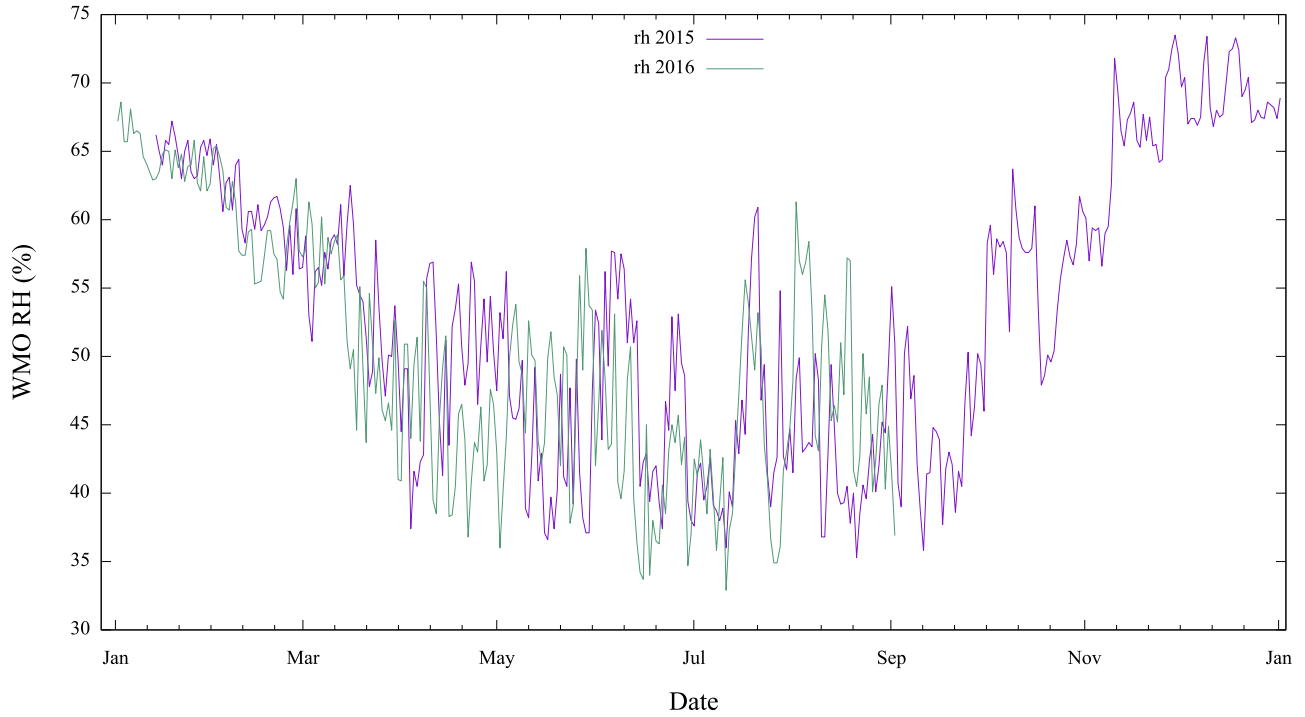


**Figure 17.** Daily median WMO RH during 2015 and 2016.  
(A color version of this figure is available in the online journal.)

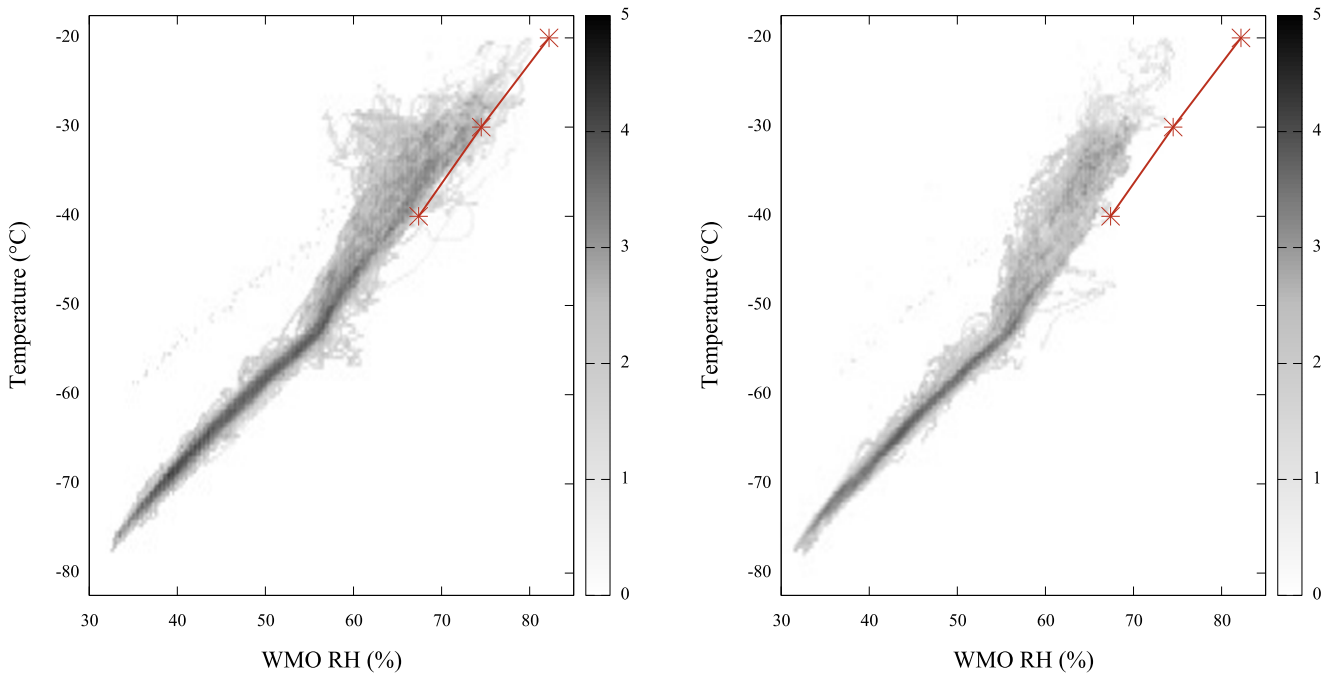


**Figure 18.** Relationship between WMO RH and temperature during 2015 (left) and 2016 (right). The gray scale is the logarithm of the number of data points in each pixel. The red line is the relationship between WMO RH and temperature when the “standard” RH is 100% given by Hardy (1998a). The strong correlation indicates the “standard” RH is close to 100% all the time.

(A color version of this figure is available in the online journal.)



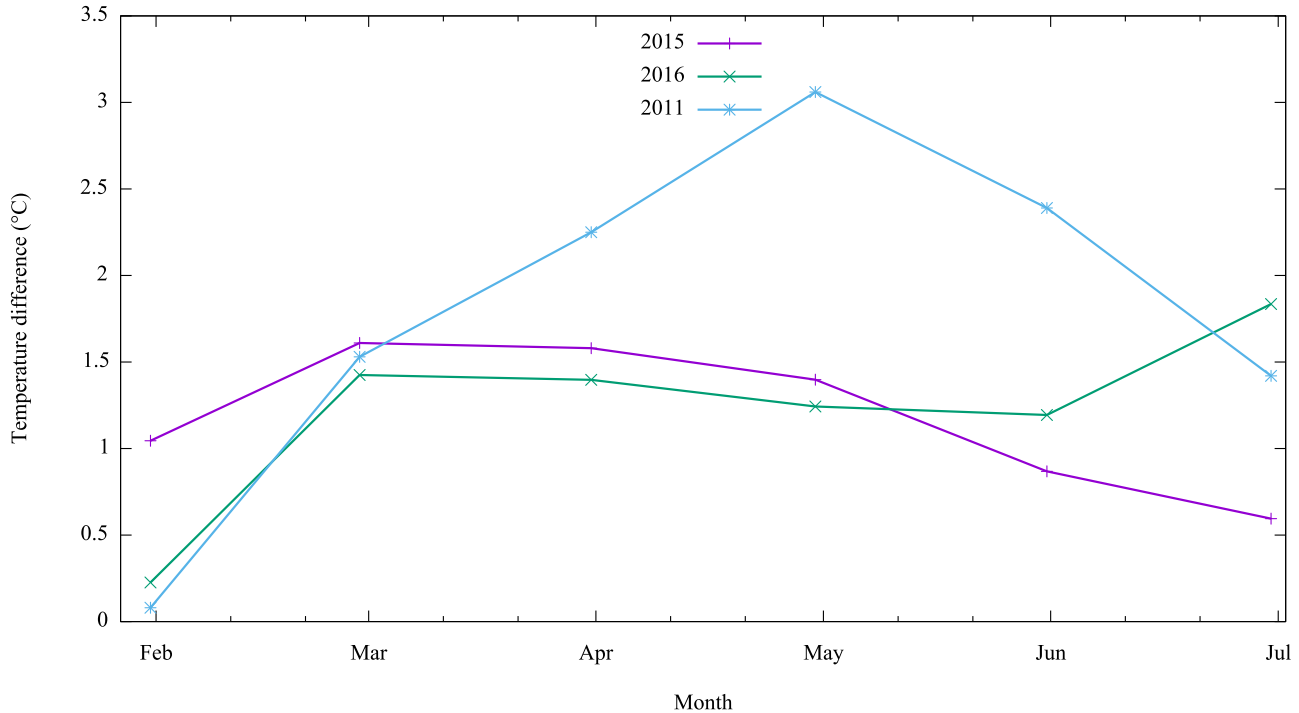


**Figure 19.** Monthly median temperature difference at 4 m during 2015 (purple), 2016 (green), and 2011 (blue). (A color version of this figure is available in the online journal.)

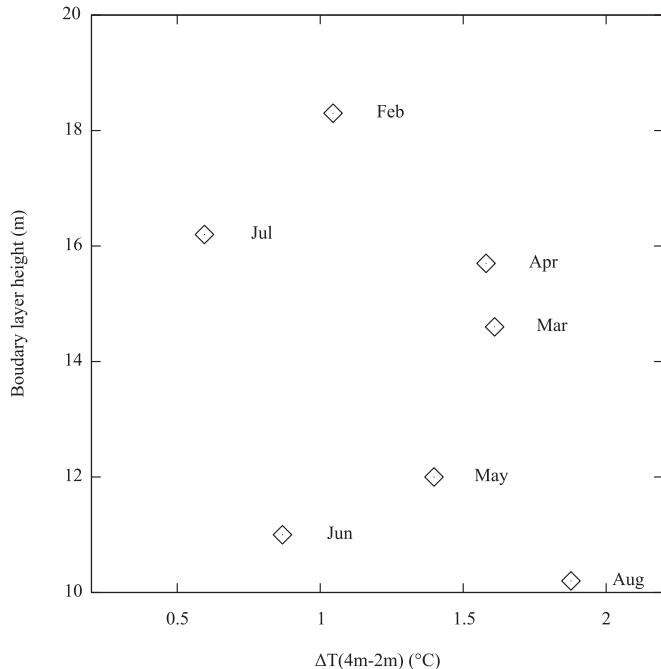


**Figure 20.** Monthly median temperature difference at 4 m in 2015 and monthly boundary layer height in 2009 (Bonner et al. 2010).

Figure 21) is somehow different from an exponential shape, since the convex-concave-convex shaped profile in the first regime also contributes to the median gradient profile. There might be a critical elevation at Dome A, above which the temperature gradient is asymptotic to positive constant. The occurrence of small positive constant temperature gradient indicates the air in that elevation tends to be in equilibrium state. This critical elevation might be the optimized height to avoid the relatively strong turbulence near the surface. As we mentioned above, the temperature gradient profile below 8 m varies significantly year by year, but the temperature gradient asymptotically approaches a constant above 8 m. Therefore, 8 m is a minimum height for building a telescope at Dome A. We will verify this with direct atmospheric seeing measurements by DIMM.

In conclusion, we find that strong temperature inversions (temperature gradient reaching up to  $7\text{ }^\circ\text{C m}^{-1}$  at 4 m) existed for all the heights above the ground at Dome A during 2015 and 2016. The temperature inversion, along with a moderate wind speed (averagely  $4.2\text{ m s}^{-1}$ ), produces a shallow boundary layer. It would imply that there will be a considerable percentage of time when a telescope that is placed just 8 to 10 m above the ground can obtain superior free-atmospheric seeing.

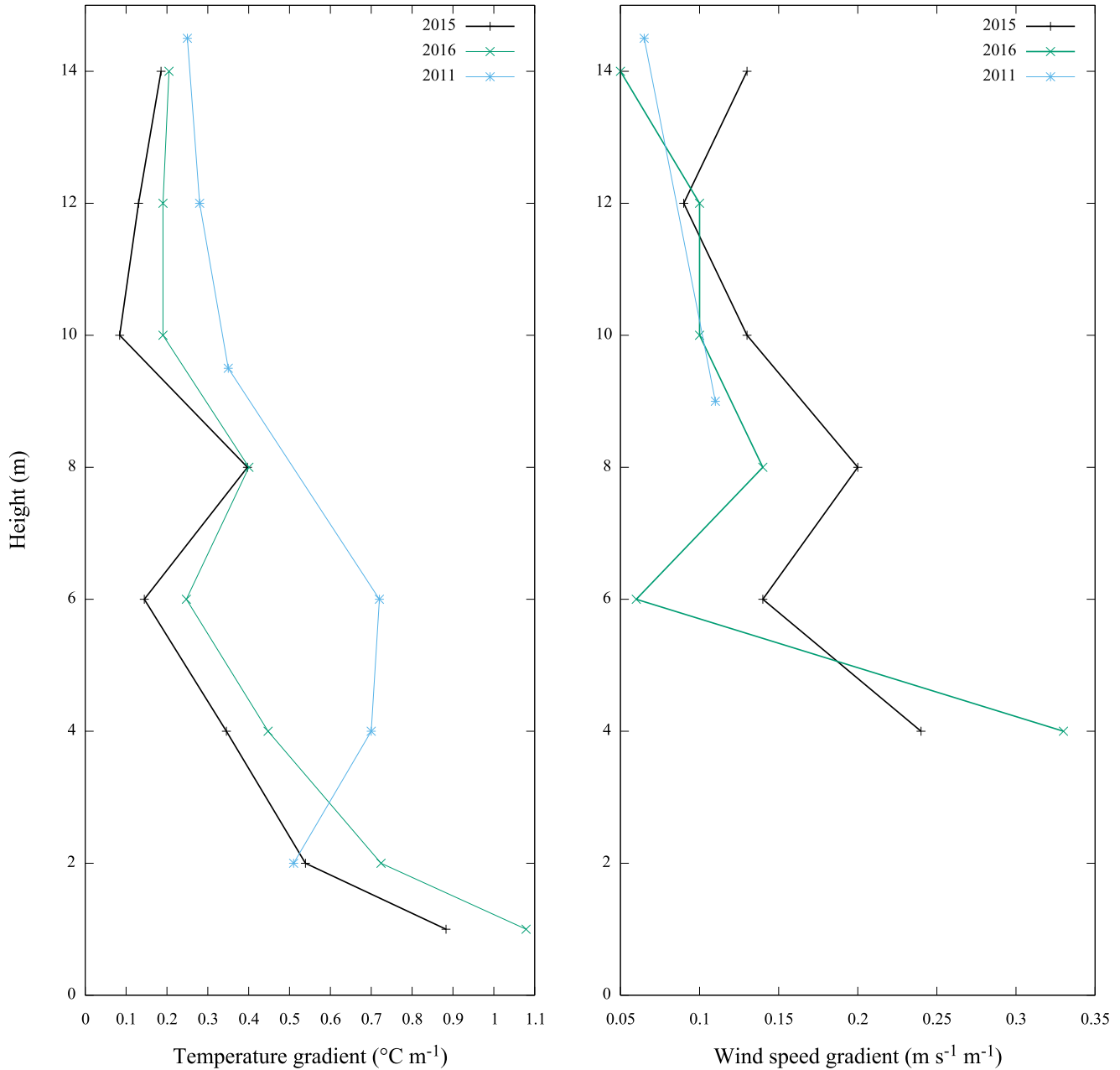


**Figure 21.** Left panel: temperature gradient profile. Right panel: wind speed gradient profile. The temperature gradients are calculated by corrected temperature at 10 m after 1 October 2015 (see Section 3.1). (A color version of this figure is available in the online journal.)

However, the complex temperature and wind-speed gradient profiles imply that small-scale simulation should be performed for studying the turbulence below the boundary layer. Also, comparing with data from KLAWS in 2011, we find annual variations in temperature, temperature inversion and wind speed at Dome A. Therefore, long-term and continuous data are

needed for thoroughly understanding the site characteristics at Dome A. We plan to install a new identical KLAWS-2G for long-term monitoring at Dome A in early 2019.

The data from KLAWS-2G during 2015 and 2016 are available at <http://aag.bao.ac.cn/klaws/downloads> and as plots at <http://aag.bao.ac.cn/klaws>.

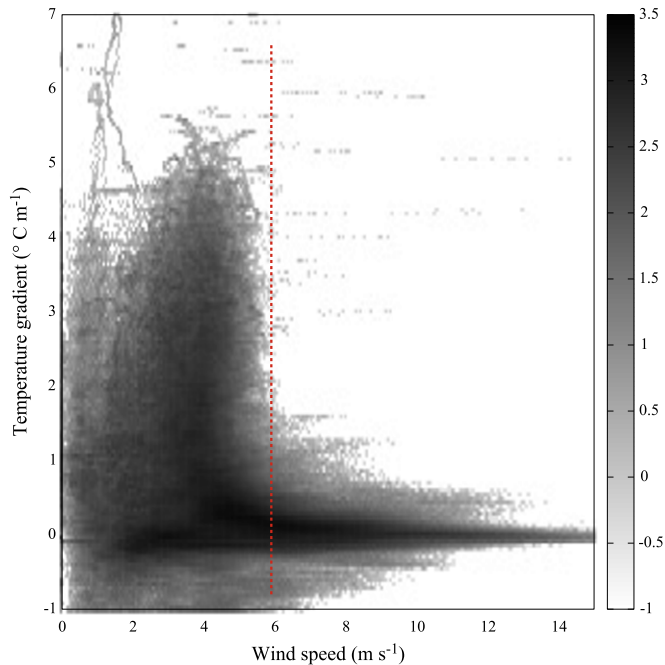


**Figure 22.** Wind speed at 4 m vs. temperature gradient at 4 m. The gray scale is the logarithm of the number of data points per pixel. The vertical red dash line at  $6.0 \text{ m s}^{-1}$  indicates the threshold wind speed.

(A color version of this figure is available in the online journal.)

The authors thank all members of the 31st, 32nd, and 33rd Chinese Antarctic Research Expedition teams for their effort in setting up the KLAWS-2G instruments and servicing the PLATO-A observatory. This research is supported by the National Natural Science Foundation of China under grant Nos.

11403048, 11733007, and 11673037, the Chinese Polar Environment Comprehensive Investigation & Assessment Programmes under grant No. CHINARE2016-02-03, the National Basic Research Program of China (973 Program 2013CB834900), the Australian Antarctic Division, and the Australian National Collaborative Research Infrastructure Strategy administered by Astronomy Australia Limited.

## References

- Aristidi, E., Agabi, K., Azouit, M., et al. 2005, *A&A*, **430**, 739  
 Aristidi, E., Fossat, E., Agabi, A., et al. 2009, *A&A*, **499**, 955  
 Bonner, C. S., Ashley, M. C. B., Cui, X., et al. 2010, *PASP*, **122**, 1122  
 Burton, M. G. 2010, *A&ARv*, **18**, 417  
 Falvey, M., & Rojo, P. M. 2016, *ThApC*, **125**, 841  
 Hardy, B. 1998a, Determination of Relative Humidity in Subzero Temperatures (Albuquerque, NM: RH Systems)  
 Hardy, B. 1998b, in Papers and Abstracts from the Third Int. Symp. on Humidity Moisture (London), **1**, 214  
 Hu, Y., Shang, Z., Ashley, M. C. B., et al. 2014, *PASP*, **126**, 868  
 Hudson, S. R., & Brandt, R. E. 2005, *JCLim.*, **18**, 1673  
 Lawrence, J. S., Allen, G. R., Ashley, M. C. B., et al. 2008, *Proc. SPIE*, **7012**, 701227  
 Lawrence, J. S., Ashley, M. C. B., Tokovinin, A., & Travouillon, T. 2004, *Natur*, **431**, 278  
 Liu, Q., Wei, P., Shang, Z.-H., Ma, B., & Hu, Y. 2018, *RAA*, **18**, 005  
 Marks, R. D., Vernin, J., Azouit, M., et al. 1996, *A&AS*, **118**, 385  
 Mohr, P. J., Newell, D. B., & Taylor, B. N. 2016, *RvMP*, **88**, 035009  
 Okita, H., Ichikawa, T., Ashley, M. C. B., Takato, N., & Motoyama, H. 2013, *A&A*, **554**, L5  
 Preston-Thomas, H. 1990, *Metro*, **27**, 3  
 Saunders, W., Lawrence, J. S., Storey, J. W. V., et al. 2009, *PASP*, **121**, 976  
 Shang, Z., Hu, K., Hu, Y., et al. 2012, *Proc. SPIE*, **8448**, 844826  
 Swain, M. R., & Gallée, H. 2006, *PASP*, **118**, 1190  
 Travouillon, T., Aristidi, E., Fossat, E., et al. 2008, *Proc. SPIE*, **7012**, 70124B  
 Vignon, E., van de Wiel, B. J. H., van Hooijdonk, I. G. S., et al. 2017, *QJRMS*, **143**, 1241  
 Zhou, M., Zhang, Z., Zhong, S., et al. 2009, *JGR*, **114**, 1673